GPPS | JOURNAL

JOURNAL OF THE GLOBAL POWER AND PROPULSION SOCIETY
journal.gpps.global

Effect of protrusions and leading edge ribs on the local heat transfer characteristics in a two-pass cooling channel under rotation

Original article

Article history:
Submission date: 4 November 2024
Acceptance date: 29 April 2025
Publication date: 24 July 2025

Check for updates

*Correspondence:
DG: david.dearcos@itlr.uni-stuttgart.de

Peer review:
Single blind

Keywords:
convective heat transfer; turbine blade; internal cooling; rotating test rig; thermochromic liquid crystals; computational fluid dynamics

Citation:
Gutiérrez de Arcos D., Waidmann C., Poser R., von Wolfersdorf J., Jäppelt B., and Semmler K. (2025). Effect of protrusions and leading edge ribs on the local heat transfer characteristics in a two-pass cooling channel under rotation. Journal of the Global Power and Propulsion Society. 9: 104–116.
https://doi.org/10.33737/jgpps/204535

OPEN ACCESS

David Gutiérrez de Arcos[1,*], Christian Waidmann[1], Rico Poser[1], Jens von Wolfersdorf[1,†], Bernhard Jäppelt[2], Klaus Semmler[2]

[1]*ITLR, University of Stuttgart, Pfaffenwaldring 31, 70569 Stuttgart, Germany*
[2]*MTU Aero Engines AG, Dachauer Str. 665, 80995 Munich, Germany*
[†]*Deceased before publication of the manuscript*

Abstract

Optimised internal cooling schemes for turbine blades aim at enhancing the heat transfer between the hot channel walls and the relatively cold fluid while preventing overcooling. Often, a combination of different turbulator types adapted to the specific turbine blade application are required. Prior research has demonstrated that a promising design featuring high heat transfer in exchange for a reasonable pressure loss penalty is achieved through the use of ribs and protrusions. As regards to rotor blades, rotation represents a key factor with a pronounced impact on the secondary flow field, and thus on the heat transfer characteristics. In the present work, local heat transfer measurements using the transient thermochromic liquid crystal (TLC) technique are conducted under engine-similar test conditions in the rotating rig of the Institute of Aerospace Thermodynamics (ITLR) at the University of Stuttgart. A two-pass cooling channel channel with two different turbulator designs is investigated: a ribbed geometry (baseline) and a rib-protrusion geometry with leading edge ribs (enhanced). Additionally, numerical simulations performed with ANSYS CFX support the experimental approach and complement it with flow field visualisations. It is shown that the rib-protrusion compound is able to improve the heat transfer under both rotating and non-rotating conditions. Nevertheless, a strong reduction in heat transfer caused by rotation occurs with the rib-protrusion geometry, especially considering the radially inward flow of the second passage. The importance of rotation on the secondary flow field and thereby on the internal heat transfer is demonstrated, contributing to a better understanding of cooling air usage under engine-realistic test conditions.

Introduction

A common approach to improve the thermal efficiency is by further increasing the turbine entry temperature. Engine components such as turbine blades are directly affected by higher thermal stresses and need to be cooled internally with bleed air. This has led to sophisticated multi-pass cooling designs in which a balance between the reduction of coolant consumption and sufficient cooling to prevent a decrease in lifespan is pursued. A thorough understanding of the underlying heat transfer processes under engine-similar conditions will unlock the potential for optimised designs with lower fuel consumption and will result in more efficient and thus sustainable aero engines. As regards to turbine blades, rotation leads to Coriolis and centrifugal buoyancy forces which alter the secondary flow field within the cooling channel (Han, 2013). This results in a different heat transfer pattern for the pressure and suction sides of the channel compared with the non-rotating frame, consequently overcooling one channel side and overheating the opposite side, depending on the radial outflow or inflow of the passage.

The recent review by Ekkad and Singh (2021a) identified the knowledge gap left by the classical temperature measurement approach based on heated copper segments, which can only provide area-averaged data. Meanwhile, more advanced thermal diagnostic techniques, such as transient liquid crystal thermography, can address this limitation and have been validated against steady-state methods (Lorenzon and Casarsa, 2020), confirming its reliability as it gains popularity within the gas turbine cooling community (see Ekkad and Singh (2021b)). In this context, Waidmann et al. (2016) presented a novel rotating rig facility (RotRig) to investigate convectively cooled turbine blades through the application of thermochromic liquid crystals (TLC). In Waidmann et al. (2018) two-dimensional heat transfer results under rotating conditions were introduced for the first time. Building upon the aforementioned work, new data reduction methods consisting of line-averaging and region-based heat transfer histograms were presented by Waidmann et al. (2022) and applied in Gutiérrez de Arcos et al. (2022) in a case study under different channel orientations and rotation numbers. The later studies were expanded in Gutiérrez de Arcos et al. (2024) with enhanced data representation methods and an experimental uncertainty estimation. Considering purely numerical investigations on internal cooling channels under rotation, Göhring et al. (2016) obtained accurate heat transfer predictions using RANS with the shear stress transport (SST) turbulence model in combination with the curvature correction and reattachment modification options available in ANSYS CFX for a benchmark case from literature (Wagner et al., 1991). Later, they expanded their investigation by assessing the time-changing buoyancy effects from the experiment and their impact on heat transfer with an URANS approach (Göhring et al., 2018). These studies demonstrate that relatively modest RANS/URANS models continue to be suitable for supporting effectively experimental methods and are still the preferred choice in the industrial sector, even after the recent attention surrounding more sophisticated numerical methods, such as LES or DNS. In terms of the application of compound heat transfer enhancement structures, Shen et al. (2015) assessed the effect of rib-dimple and rib-protrusion turbulators under rotating conditions. The rib-protrusion geometry exhibited the best heat transfer rates for a reasonable pressure loss penalty, reaching the highest thermal performance for all considered rotation numbers. Nevertheless, this investigation was limited to a purely numerical study.

The key aims of this paper are to describe and quantify the changes in the local heat transfer of a ribbed leading edge with a rib-protrusion cooling feature in the second passage (enhanced) and to compare it with the ribbed channel (baseline). Particularly, we seek to clarify the impact of rotation on heat transfer rates for the enhanced design, which, according to published research, promises a remarkable improvement in the cooling effect. To this end, we apply the transient TLC technique and complement it with CFD results from a RANS model, which is validated here.

Experimental approach

Conducting heat transfer experiments for internal flows under engine-similar rotating conditions is a challenging task, particularly considering the need to capture local effects. Such effects are inherent to the geometry and operating point and can only be acquired via specific measurement techniques. In the following sections, the most relevant aspects about the rotating test rig, the test models, and the experimental heat transfer evaluation are examined.

Rotating test rig

In Figure 1 an overview with the key components of the test rig, which was presented in detail in Waidmann (2020), is shown. In an effort to correctly reproduce the buoyancy effects from the real machine, transient TLC experiments are performed with test air below the ambient temperature. Fluid temperatures as low as −100°C can be achieved for the three air supplies (precool air, tempering air and test air) by means of a heat exchanger operated with liquid nitrogen. Prior to the start of the experiment, precool air (1) is driven through the rotary union at the right hand-side of Figure 1 and flows through the pipes in the hollow shaft and rotor arm. These act as a heat exchanger to the test air pipes, which need to be precooled to a certain temperature so as to minimise heat intake during the experiment, thus facilitating the fluid temperature step change. Tempering air (2) with a temperature equal to the measured test model temperature is directed through the rotary union at the left-hand side of the figure. It continuously flows through the test model in order to pressurise it and to hold constant its initial temperature level. When the rotor pipes reach the desired temperature and the model is pressurised, the electric motor drives the shaft through a belt drive at a speed of up to 900 rpm. Once the target rotating speed,

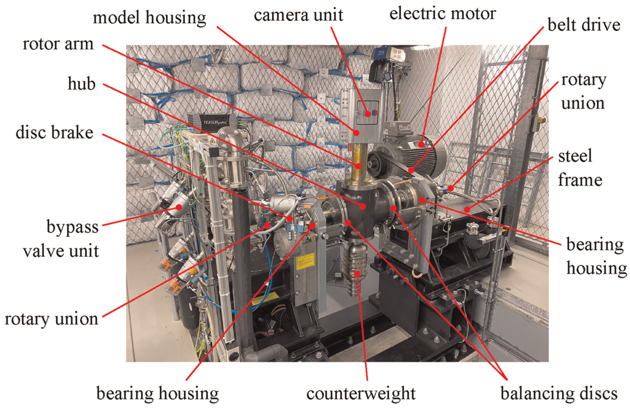

Figure 1. Overview of the rotating rig.

pressure level and test air temperature are reached, the test air (3) is driven through the test model, marking the start of the TLC experiment. This is achieved through a bypass valve unit consisting of six valves which enables the switch between the tempering air and the test air supply. The test air finally exits the shaft through the same rotary union.

The test bench was designed to enable the accurate setting of the target operating conditions. For this investigation, test cases are classified according to their Reynolds number (*Re*) and rotation number (*Ro*). The Reynolds number, determined as $Re = \dot{m}d_h/A\eta$, is computed from the cooling air mass flow, the dynamic viscosity determined at the channel inlet location TC0102 (see Figure 3) and the channel geometry. In $Ro = \rho A\Omega d_h/\dot{m}$, *Ro* represents the ratio of the rotational effects to the inertial forces and is evaluated based on the rotational speed, the channel geometry, the air density calculated from pressure and temperature measurements at the channel inlet (TC0102), and the cooling air mass flow. The test cases in this study are derived from engine-realistic conditions and their operating points are summarised in Table 1.

Test models

Baseline geometry

The baseline design has been derived from a previous work on a non-rotating test bench (Waidmann et al., 2013). The test model is made of acrylic glass in order to facilitate the optical access with cameras from the

Table 1. Operating conditions and dimensionless parameters for the present investigation.

Parameter	Variable	Value
Fluid temperature measured at the channel inlet (TC0102)	T_f	$-15.8\ldots-5.8$°C
TLC indication temperature	T_{ind}	2.38°C (baseline); 2.39°C (enhanced)
Initial wall temperature	T_w	16.7…19.7°C
Mass flow	$\dot{m}$	≈4.8 g/s
Mean model radius	$\bar{R}$	750 mm
Pressure	p	≈6 bar
Reynolds number	Re	≈15,000
Rotation number	Ro	0; ≈0.15
Rotational speed	n	0; 197 rpm

outside, and consists of two half-shells, a divider web and a tip wall. The inner channel walls are coated with TLCs and black backing paint. The geometry is comprised of a first passage (Pass 1) with a radially outward flow, a 180°-bend, and a second passage (Pass 2) with a radially inward flow. The first passage features a trapezoidal cross-section with a hydraulic diameter of $d_h = 15$ mm and represents a simplified leading edge cooling channel geometry. At the bend, the channel geometry transitions from a trapezoidal (Pass 1) to a rectangular cross-section (Pass 2). The pressure side (PS) and the suction side (SS) are equipped with staggered ribs with angles between 60° and 65°. Fluid temperature histories in the channel are measured with type K thermocouples (TC) along the geometric centerline of the flow path. Additionally, three TCs measure the temperature at various wall depths so as to guarantee isothermal starting conditions for the transient experiment.

Enhanced geometry

The enhanced design, illustrated schematically in Figure 2 (left) and with the two half-shells (right), features the same rib configuration for PS and SS as the baseline design. In an effort to improve the heat transfer in the first passage, ribs from both channel sides are extended to the leading edge (LE) with a decreasing height, resulting in a triangular shape. In the second passage, the segments (i.e., the channel wall between two consecutive ribs) of PS and SS are equipped with a pattern of 3×3 spherical protrusions and a height-to-diameter ratio of $\delta/D = 0.25$. The protrusions present a parallel arrangement respective to the adjacent ribs, as shown in Figures 2 and 3. Temperature and pressure measurements are identical to the baseline geometry.

Experimental heat transfer evaluation

The experimental method is based on the transient TLC technique, as described in Poser et al. (2007, 2005) and Ireland and Jones (2000). By means of this approach, TLCs are used as temperature sensors and their response times, i.e., indication times, are determined after a sudden fluid temperature change is applied. Through analysis of the pixel-wise TLC indication times and the fluid temperatures, local heat transfer coefficients can be calculated. In the present investigation the TLC type G0C1W with a bandwidth of 1 K from Hallcrest has been applied and calibrated with the stationary calibration method proposed in Poser and von Wolfersdorf (2010), resulting in the indication temperatures presented in Table 1 for the baseline and enhanced geometries.

Heat transfer analysis is performed by means of the in-house code ProTeIn. The first steps involve wavelet-based filtering and adaptive normalisation, as presented in Poser et al. (2009). Following, the time at which the intensity of the green colour channel reaches its maximum, i.e., the TLC indication time, is determined for each pixel separately. The fluid temperature history for each channel position is determined by means of the CFD-based method presented in Gutiérrez de Arcos et al. (2022). The heat transfer coefficient h is calculated through solution of the one-dimensional Fourier heat conduction equation for a semi-infinite solid body and convective boundary condition. However, in order to approximate the actual fluid temperature history, this needs to be discretised through tiny temperature steps $\Delta T_{f\,(j,j-1)}$, and the Duhamel superposition principle needs to be applied. That results in Equation 1:

$$T_w - T_0 = \sum_{j=1}^{N} [1 - \exp(\beta^2) erfc(\beta)] \cdot \Delta T_{f\,(j,j-1)} \quad \text{with} \quad \beta = h\sqrt{\frac{t_{\text{ind}} - \tau_{\text{j}}}{\rho_w c_w k_w}} \tag{1}$$

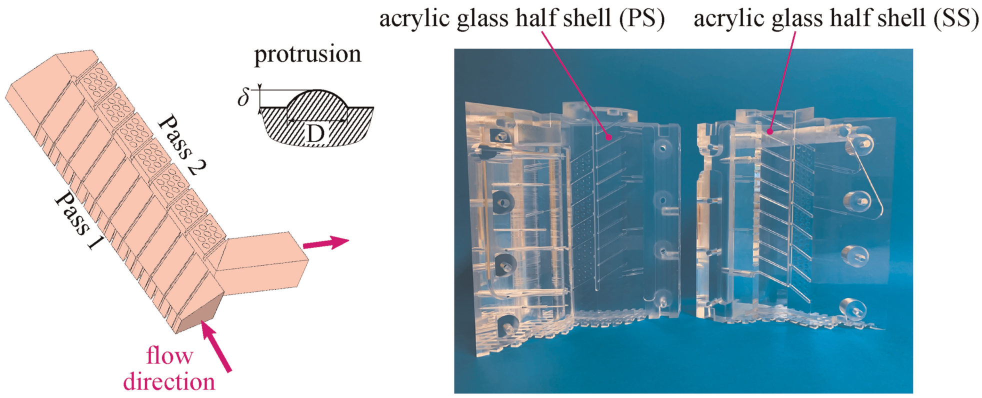

Figure 2. Schematic view of the fluid domain (left) and test model (right) of the enhanced geometry.

The wall temperature corresponds to the temperature at the time of indication t_{ind}, i.e. $T_w = T_{\text{ind}}$, and the initial temperature is given with T_0. τ_j is given by is a discrete point in time of the fluid temperature history, and ρ_w, c_w and k_w are the physical properties of acrylic glass. Heat transfer results are presented in their dimensionless form by means of the Nusselt number $\text{Nu} = h \cdot d_h / k(\overline{T_f})$ with the local thermal conductivity $k(\overline{T_f})$ evaluated for the time-averaged local fluid temperature history until the time of indication, and the hydraulic diameter of the first passage d_h.

Numerical setup

A numerical model implemented in ANSYS CFX 2021 R2 simulates the convective heat transfer in the fluid domain and supports the experimental approach where no data is available. This is the case for the leading edge of the baseline geometry, where optical access was not possible. Whereas the heat transfer experiments are of a transient nature, steady-state CFD computations have been performed. The setup has been successfully applied in previous investigations and allowed for accurate heat transfer predictions of the baseline cooling channel, as shown by Gutiérrez de Arcos et al. (2022), and in the qualitatively similar internal cooling channel under rotation presented in Göhring et al. (2018). The method is based upon the solution of the stationary Reynolds-averaged Navier-Stokes (RANS) equations in their total enthalpy form with the two-equation SST scheme by Menter (1994). Additional correction terms for the well-known delayed flow separation under adverse pressure gradients (reattachment modification) and insensitivity to streamline curvature and rotation (curvature correction) are presented in ANSYS CFX Theory guide (2021), and are applied here. The mentioned corrections have been validated in Göhring et al. (2016) and are used here due to their robustness and proven good comparability with experimental results. Air is modelled as an ideal gas and the transport properties viscosity and thermal conductivity are calculated by means of the Sutherland's equations (White and Majdalani, 2006). Regarding convergence, maximum residuals in the momentum and energy equations of $5 \cdot 10^{-3}$ are targeted, and average residuals (RMS) of $5 \cdot 10^{-4}$ are tolerated.

Boundary conditions

In Figure 3 an overview of the numerical domain with the applied boundary conditions is presented for the enhanced geometry exemplary. Fully developed flow conditions are present at the inlet. The three components of the velocity vector in Cartesian coordinates (X, Y, Z) are derived from a preceding calculation. Furthermore, the inlet temperature stems from the transient TLC experiment as an estimation of the average temperature for the duration of the experiment at the channel inlet, i.e., at the measurement location of the thermocouple pair TC0102. The outlet is characterised with a static pressure boundary condition equal to $p_{\text{out}} = 6\text{bar}$ for all numerical simulations. Considering the channel walls, the no-slip condition is set and a constant temperature equal to the starting temperature of the TLC experiment is applied. Inflow and outflow regions of the channel are modelled as adiabatic walls. Furthermore, the outlet region is extended in order to avoid interference of possible recirculation regions at the boundary location. For cases with rotation, the fluid domain is set a constant rotating speed analogous to the TLC experiment.

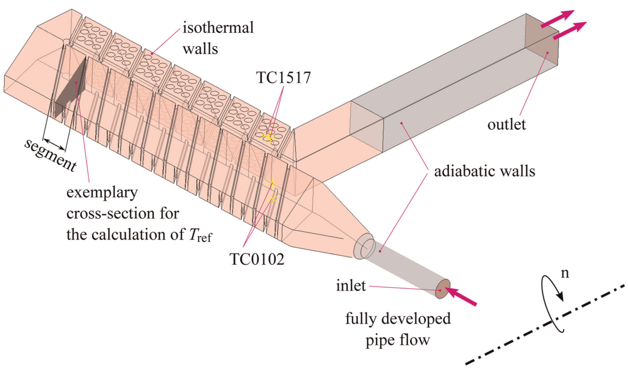

Figure 3. Boundary conditions and experimental TC locations at inlet and outlet of the cooling channel, i.e. TC0102 and TC1517, respectively.

Mesh generation and mesh independence study

The numerical grids were generated in ANSYS ICEM 17.1 (baseline geometry) and ANSYS ICEM 2021 R2 (enhanced geometry) following a multi-block structured approach. The different channel regions were modelled separately in order to allow for a better control of the desired target quality parameters, such as aspect ratio, grid angle and volume change, in accordance with the ANSYS ICEM CFD User's manual (2021), and dimensionless distance of the first cell adjacent to the wall. In regard to heat transfer, high quality meshes with well-resolved near-wall regions are required. The dimensionless wall distance must not exceed $y_1^+ \approx 1$ in order to fully resolve the wall-adjacent region. Furthermore, the cell growth rate perpendicular to the wall is carefully chosen so as to ensure a smooth transition from the walls to the core flow.

On the basis of the aforementioned constraints, a mesh independence study was conducted for the enhanced geometry, following the method proposed in Celik et al. (2008). Through this approach, the Grid Convergence Index (GCI), initially introduced by Roache (1994), is calculated and delivers an estimation for the grid discretisation error of a desired target variable. Three different grids (fine, medium, coarse) with a refinement factor of at least 1.3 are needed, while the first wall cell height is held constant. The study was performed for the area-averaged Nusselt number at the PS, SS and LE channel walls. Depending on the considered channel segment, area-averaged uncertainties can be as high as $\mathrm{GCI}_{\max} = 9.7\%$ at PS, $\mathrm{GCI}_{\max} = 11.1\%$ at SS, and $\mathrm{GCI}_{\max} = 13.1\%$ at LE for the fine grid. For the most part of the cooling channel, however, area-averaged uncertainties are below $\mathrm{GCI} = 5\%$. The final meshes consist of 11.7 (baseline) and 19.0 million grid nodes (enhanced).

Numerical heat transfer evaluation

Convective cooling is quantified by means of the heat transfer coefficient calculated with Newton's law (Incropera et al., 2017) with

$$h = \frac{\dot{q}_w}{(T_w - T_{\mathrm{ref}})} \tag{2}$$

and is made dimensionless with the Nusselt number. In Equation 2 the wall temperature T_w is set as boundary condition in the numerical model and the specific wall heat flux $\dot{q}_w$ is a direct result from the numerical simulation. In regard to the Nusselt number $\mathrm{Nu} = hd_\mathrm{h}/k(T_{\mathrm{ref}})$, the hydraulic diameter of the first passage d_h is used and is identical for both considered geometries, and the thermal conductivity $k(T_{\mathrm{ref}})$ is calculated at each PS, SS and LE segment for the corresponding reference temperature. The reference temperatures T_{ref} for each PS, SS and LE segment are determined at the corresponding cross-sectional location, defined as the midpoint between the inlet and outlet of each channel segment (see an exemplary segment with its corresponding cross-section in Figure 3). With knowledge of the numerically-obtained bulk temperatures along the cooling channel a dimensionless temperature profile is derived, which is then used to correct the measured fluid temperatures of the TLC experiment through the procedure presented in Gutiérrez de Arcos et al. (2022).

Results and discussion

In the following sections, heat transfer results are presented as the ratio of the local Nusselt number to the corresponding Nusselt number from the Dittus-Boelter/McAdams correlation (Williams, 2011) for fully developed turbulent pipe flow, $\mathrm{Nu}(x, y)/\mathrm{Nu}_0$, defined as $\mathrm{Nu}_0 = 0.023\,\mathrm{Re}^{0.8}\mathrm{Pr}^{0.4}$. Physical properties for the determination of both dimensionless parameters, Re and Pr, are determined at the channel inlet location TC0102. The exponent 0.4 for the Prandtl number can be used for cooling experiments, i.e., experiments in which the fluid flow is colder than the channel walls, and is therefore applied here. In order to assess the rotational effects on heat transfer, the normalised Nusselt number ratio (*NNNR*) from the rotating to the non-rotating case, $\mathrm{NNNR}(x, y) = (\mathrm{Nu}(x, y)/\mathrm{Nu}_0)_{\mathrm{ROT}}/(\mathrm{Nu}(x, y)/\mathrm{Nu}_0)_{\mathrm{STAT}}$, is used.

CFD validation

Experimental (EXP) and numerical (CFD) local heat transfer rates are depicted in Figure 4 and have been obtained for the baseline geometry with and without rotation, i.e., at $Ro \approx 0.15$ and $Ro = 0$, respectively. They show the heat transfer enhancement relative to the non-ribbed cooling channel from the Dittus-Boelter/McAdams correlation for PS, LE and SS. The flow direction is highlighted at inlet and outlet of the channel with black arrows. In case of the TLC experiment, data for LE is not available. Ribs and the inner wall separator

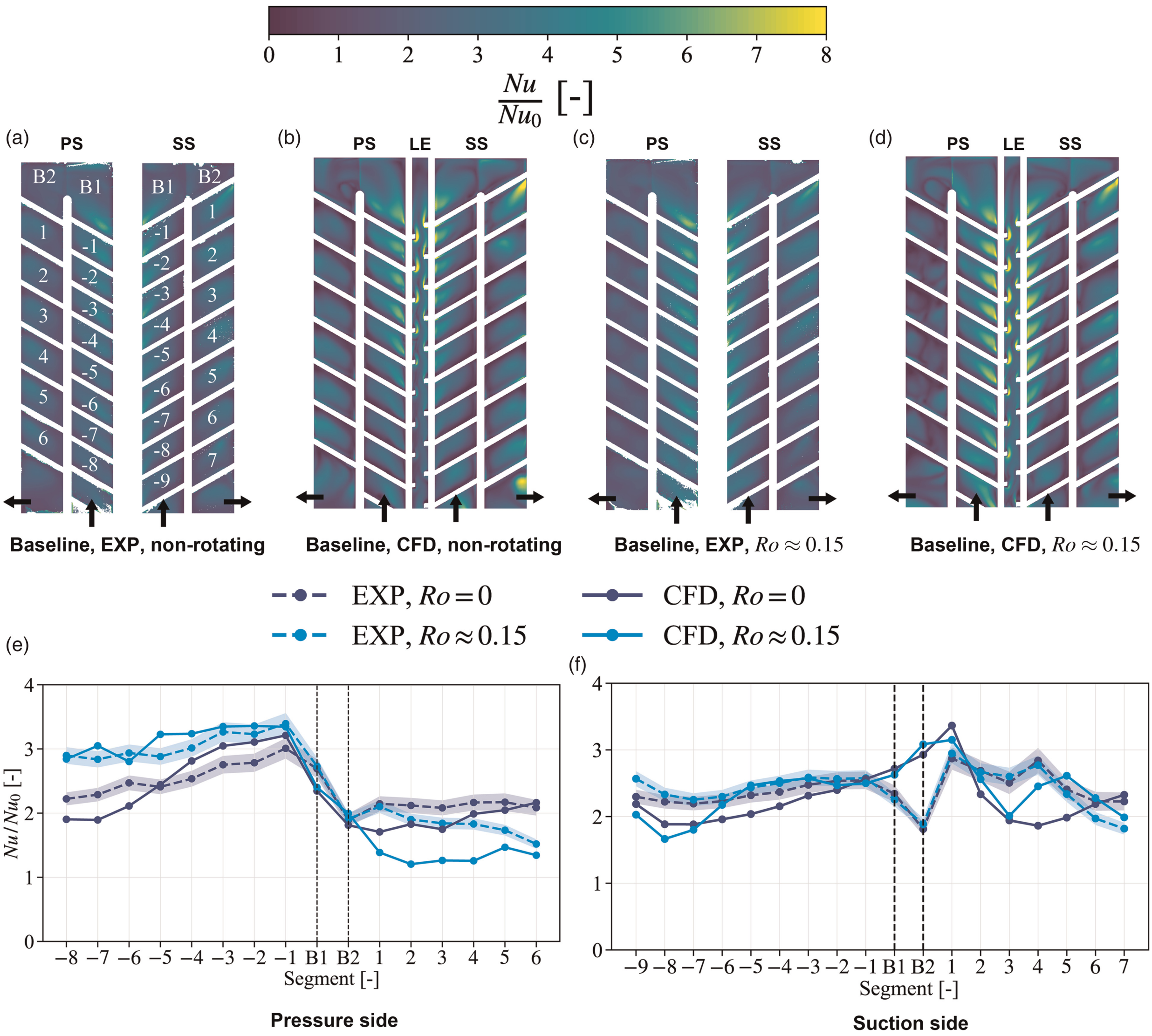

Figure 4. Experimental and numerical heat transfer structure (a–d) and segment-averaged heat transfer (e and f) for the baseline geometry under rotation ($Ro \approx 0.15$) and without rotation.

between the first and the second passages (corresponding to a radially outward and a radially inward flow, respectively) have been blanked out.

The non-rotating case, displayed in Figure 4a and b, features a heat transfer level that appears to increase towards the bend for the three considered channel regions. From inlet towards bend, a flow pattern consisting of detachment and reattachment to the wall caused by the angled ribs is repeated, as it can be appreciated from both, experimental and numerical results. Moreover, the trapezoidal shape of the first passage translates into generally higher heat transfer for PS than for SS. Directly downstream of the bend, a streak with high heat transfer rates is visible at the first segment of SS as a result of the 180°-turn, which triggers the cooling air impingement onto the SS wall. This structure is visible for both experiment and CFD simulation, however, in the experimental results the streak appears to be weaker in terms of heat transfer level. With disregard to the later point, the second passage is characterised by a monotonous heat transfer structure for PS and SS, and experimental and CFD results align qualitatively well.

As the cooling channel is set under rotation additional sources of momentum arise, altering the secondary flow field and ultimately impacting on the local heat transfer structure. In Figure 4c and d contour plots of the local heat transfer under rotating conditions ($Ro \approx 0.15$) are presented for experiment and CFD, respectively. Considering the local structures of the first passage, little change can be observed in comparison with the non-rotating case. Similar to the non-rotating case, heat transfer rates increase towards the bend for the three considered channel regions. There only appear to be changes in the heat transfer level, with a clear enhancement in the rotating case. In contrast to the first passage, the PS second passage features a distinctive pattern which is correctly reproduced by the numerical model, and displays generally lower heat transfer rates than in the non-rotating case. Overall, the qualitative agreement between experimental and numerical results is satisfactory. In order to quantify the deviations between TLC experiments and numerical simulations, data from the contour plots in Figure 4 has been segment-averaged and is displayed at the bottom of Figure 4 by means of XY-plots for PS (left) and SS (right). The flow direction is from left (−8 or −9 at the inlet, respectively) to right (6 or 7 at the outlet, respectively) and the corresponding naming for the different segments is given in Figure 4a. Whereas experimental data is plotted with dashed lines and the respective band with the uncertainty estimation, CFD data is plotted by means of solid lines. At first glance, the main trends observed in the experiment are mirrored appropriately by the CFD data. Considering both experimental and numerical results for the first passage of PS, a deviation below ±12% is reached for the majority of the segments, with the highest discrepancies of −18% for segment −7 in the non-rotating case. Considering the second passage of PS, heat transfer for the rotating case is drastically under-predicted by the CFD, yet a relatively good agreement is reached for the non-rotating case. With respect to the SS, the maximum deviation from the experimental results occurs at B2 and reaches +62% for the non-rotating and +64% for the rotating case, generally with a discrepancy bandwidth smaller than ±20%.

Regarding the enhanced geometry, experimental data for LE is available and can be therefore compared directly with the CFD results in Figure 5 for the rotating case $Ro \approx 0.15$, exemplary. In this case, the triangular ribs induce a pattern of diagonal streaks of increased heat transfer for all visible segments. Apparently, their particular shape result in the flow being deflected with a certain angle towards the LE wall, thereby creating a distinguishable heat transfer structure and improving the cooling effect. Analogous to PS and SS for the baseline geometry, heat transfer rates at LE increase from inlet towards bend. They do it in a particular *zigzag* manner, i.e., higher heat transfer rates for *B*-segments (e.g. −1B, −2B, −3B, etc.) than for *A*-segments, as indicated by the segment-averaged data in Figure 5c. A possible explanation for this phenomenon might be given by the trapezoidal cross-sectional shape of the first passage with angled ribs which, in combination with the rotational effect, deflects the flow field from PS to SS, washing the LE. The highest deviation from experimental data occurs at segment B1. In this case, however, due to optical difficulties, the experimental data covers less than half of the considered segment and must be therefore handled with caution. The same applies to segments −8A, −8B, −9A and −9B, which have been blanked out due to insufficient experimental data to draw conclusions. For most of the segments at the LE, the CFD deviation from experimental results falls within a ±15% band, which can be regarded as satisfactory.

Rotationally-induced heat transfer

The integration of leading edge ribs and protrusions in the second passage is expected to alter the secondary flow field and thereby result in heat transfer enhancement. In Figure 6d and e, local heat transfer is depicted in form

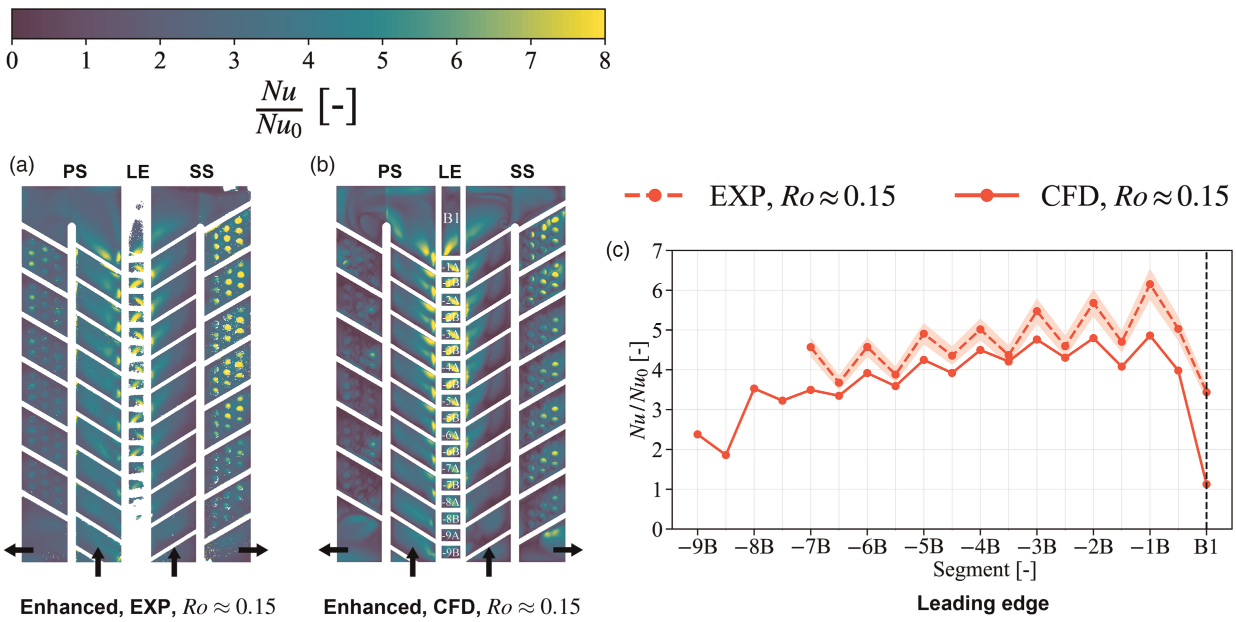

Figure 5. Experimental and numerical heat transfer structure (a and b) and segment-averaged heat transfer (c) for the enhanced geometry under rotation ($Ro \approx 0.15$).

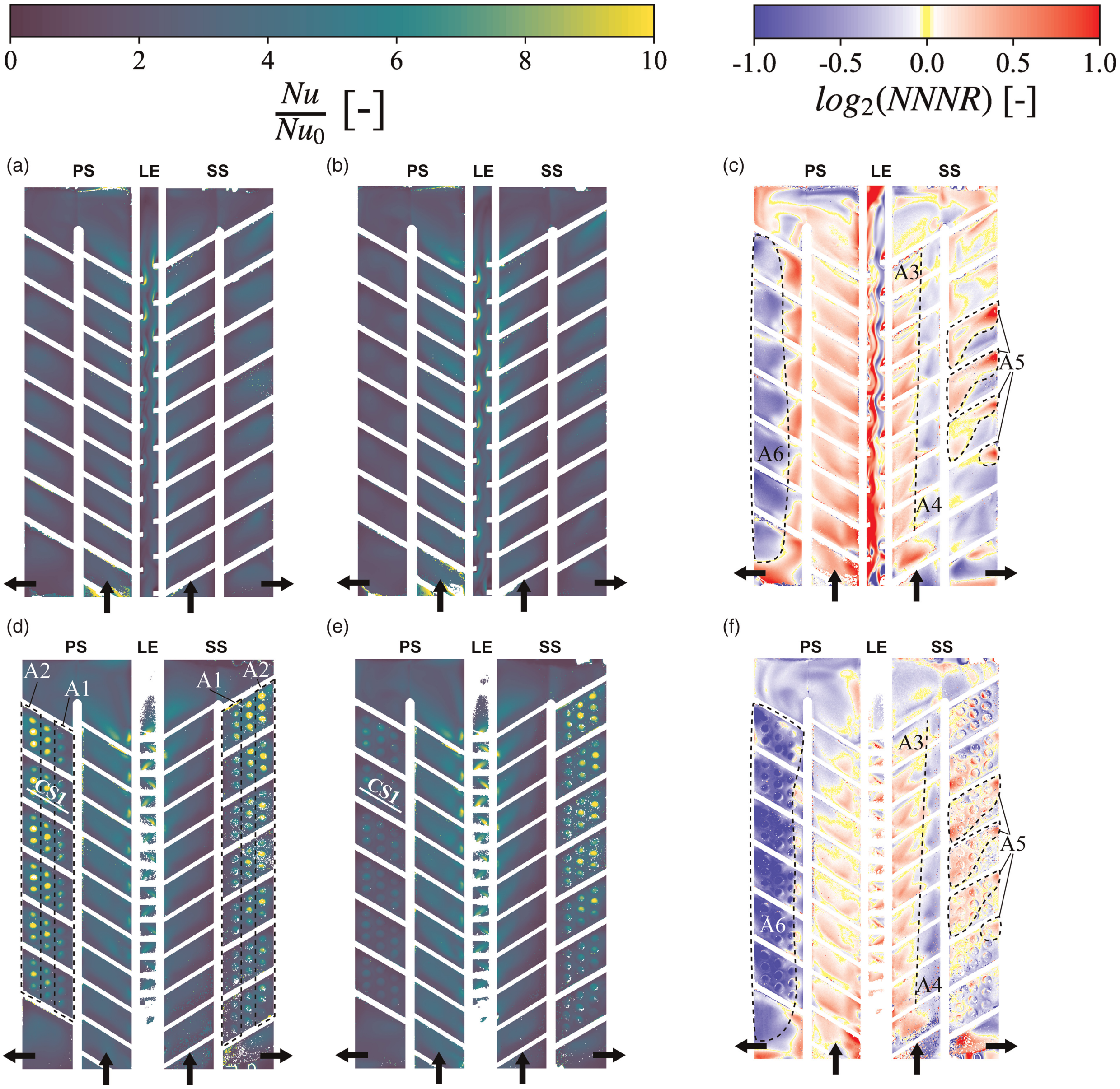

Figure 6. Experimental heat transfer structure for the baseline (top) and enhanced geometries (bottom) under rotation ($Ro \approx 0.15$) and without rotation. LE data for the baseline case stems from the CFD. (a) Baseline, non-rotating (b) Baseline, $Ro \approx 0.15$ (c) Baseline, $Ro \approx 0.15$ (d) Enhanced, non-rotating (e) Enhanced, $Ro \approx 0.15$ (f) Enhanced, $Ro \approx 0.15$.

of $\mathrm{Nu}(x, y)/\mathrm{Nu}_0$ contour plots for the enhanced geometry in the non-rotating and rotating case ($Ro \approx 0.15$), respectively. For a direct comparison, results from Figure 4 for the baseline geometry are displayed again in Figure 6a and b. LE data for the baseline geometry stems from the CFD simulation results. Considering the non-rotating case, a strong increase relative to the baseline geometry is visible for the second passage of PS and SS, with pronounced peaks at the locations of the protrusions, especially at their windward surface. As a consequence of the channel symmetry, both channel sides appear to be similarly affected by the change in the secondary flow field due to protrusions. Likewise, both sides display lower heat transfer rates in the regions adjacent to the inner wall separator (A1), which increase towards the rear side of the channel with the highest peaks at the locations of the protrusions (A2). Through incorporation of LE ribs as an extension of the turbulators at PS and SS, the heat transfer structure completely changes, as observed by comparing Figure 6a and d.

Under the presence of rotation the resemblance between PS and SS in the second passage of the enhanced geometry vanishes. Heat transfer rates remain high for SS, whereas they decrease drastically for PS. This is triggered by the governing Coriolis force direction, which deflects the cooling air from PS towards SS for the radially inward flow. The effect manifests itself in the secondary flow field visualisation from Figure 7, where in-plane velocity vectors in the PS near-wall region over the protrusions are depicted. The corresponding cross-sectional

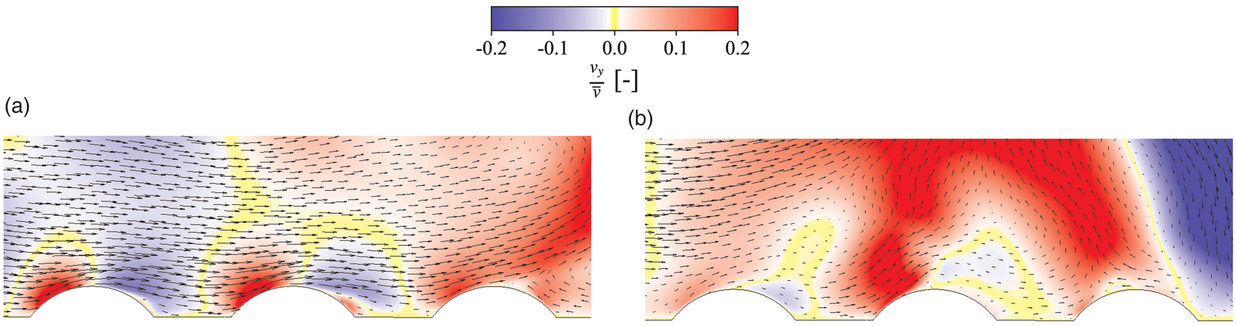

Figure 7. Detailed view CS1 (see Figure 6d and e) of the secondary flow field structure in the PS near-wall region for the enhanced geometry. (a) Non-rotating (b) Ro ≈ 0.15.

location (CS1) is indicated with a white line in Figure 6d and 6e. Additionally, the wall-perpendicular velocity component v_y has been normalised with the average velocity of the plane (same value for rotating and non-rotating cases) and is displayed as contour plot. The sign, e.g. positive for air flowing towards the protrusions at SS, and magnitude of the vertical velocity component are revealed through application of a divergent colour legend. In the rotating case, the velocity vectors show considerably lower near-wall velocity gradients than in the non-rotating case. Furthermore, in the presence of rotation the Coriolis force lifts the air from the wall, directing to towards the opposite side (SS) and contributing to a reduced heat transfer level at the PS. A similar effect can be assumed for the baseline geometry. The rotational effect can be more clearly visualised through the use of the normalised Nusselt number ratio with a logarithmic scale to the basis of 2. Thereby, the enhancing and diminishing effect of rotation on heat transfer is revealed. In Figure 6c and f contour plots of $\log_2$(NNNR) for the baseline and enhanced geometries, respectively, are depicted. Rotationally-induced heat transfer enhancement is displayed in red; and rotationally-induced heat transfer decrease is displayed in blue. Yellow areas indicate little to no sensitivity to rotation. Whereas variation in the local heat transfer level and structure due to rotation between both geometries for SS is very limited (see A3, A4 and A5), the second passage of PS experiences a remarkable heat transfer decrease (A6), which is in agreement with the lower near-wall velocities noted previously for the rotating case. Furthermore, the rib-protrusion compound of the enhanced geometry intensifies this negative effect, as revealed by the contour plots. Considering the first passage of PS, a lower dependency on rotation exists for the enhanced geometry, as evidenced by the milder rotationally-induced heat transfer pattern. Focusing on the LE of the baseline geometry, a *stream* of increased heat transfer due to rotation develops from inlet towards bend, with the highest rotationally-caused increase at the channel inlet. The local structure changes completely for the enhanced geometry, where segment-wise *zigzag*-shaped streaks of increased heat transfer from inlet to bend are observed, with an overall milder rotational effect, compared with the baseline case.

Summary and conclusions

This paper demonstrates the potential benefits of LE ribs and protrusions in combination with angled ribs for turbine blade internal cooling. First, a numerical model based on stationary CFD simulations is validated against transient TLC experimental data, exhibiting a noteworthy agreement. Hence, the model qualifies for supporting the experiment at the LE of the baseline cooling channel, where no experimental data could be obtained. A qualitative assessment of heat transfer data through contour plots reveals the changes in the local heat transfer structure with the incorporation of the additional turbulators. This alteration results in an overall higher heat transfer level under both rotating and non-rotating conditions, compared with the baseline geometry, i.e., ribbed channel. The examination of the presented data leads to the following key conclusions:

- Under non-rotating conditions, a remarkable local heat transfer enhancement is evident at the location of the protrusions for PS and SS, with an overall higher heat transfer level than in the baseline case.
- Under rotating conditions, the local heat transfer enhancement at the location of the protrusions for PS was marginal compared with the baseline geometry. Contrarily, the heat transfer level increased significantly for the protrusions at SS.
- Under both non-rotating and rotating conditions, the integration of LE ribs as an extension of PS and SS ribs implies a beneficial effect on the heat transfer at the LE area, though it is not quantified here.

- The isolated impact of rotation on heat transfer ranged from a slightly positive effect (PS first passage) to a substantially negative effect (PS second passage) in terms of heat transfer augmentation for the enhanced geometry. The secondary flow field visualisations from the CFD supported the heat transfer results and unveiled the reduction of near-wall velocities for the second passage of PS in the presence of rotation. Compared with the baseline geometry, the overall gain through rotation decreased, especially for the second passage of PS. Little variation was observed for SS.

In the present investigation the suitability of the proposed blended experimental-numerical approach has been confirmed. The reported findings underscore the importance of conducting locally-resolved heat transfer investigations under engine-relevant rotating conditions. The local effects inherent to specific turbulator geometries for diverse operating points should not be neglected, since they could potentially lead to further improvements in the cooling efficiency if considered in the turbine blade design process.

Nomenclature

Symbol	Description (Unit)

Latin symbols

c_P	Specific heat capacity at constant pressure (J/(kgK))
D	Protrusion diameter (mm)
d_h	Hydraulic diameter (mm)
h	Heat transfer coefficient (W/(m^{2}K))
k	Thermal conductivity (W/(mK))
$\dot{m}$	Mass flow rate (g/s)
n	Rotational speed (rpm)
NNNR	Normalised Nusselt Number Ratio (–)
Nu	Nusselt number (–)
Nu_0	Nusselt number from Dittus-Boelter correlation (–)
p	Pressure (bar)
Pr	Prandtl number (–)
$\bar{R}$	Mean model radius (mm)
Re	Reynolds number (–)
Ro	Rotation number (–)
t	Time (s)
T	Temperature (°C)
y_1^+	Dimensionless wall distance of the first node (–)

Greek symbols

δ	Protrusion height (mm)
η	Dynamic viscosity (kg/(ms))
ρ	Density (kg/m^3)
τ	Timestep (s)
Ω	Rotational speed (rad/s)

Indices

$\square_0$	Initial
$\square_\mathrm{f}$	Fluid
$\square_\mathrm{ind}$	Indication
$\square_\mathrm{in}$	Inlet, i.e. at thermocouple position TC0102
$\square_\mathrm{max}$	Maximum
$\square_\mathrm{out}$	Outlet, i.e. at thermocouple position TC1517
$\square_\mathrm{ref}$	Reference
$\square_\mathrm{ROT}$	Rotating

$\square_{STAT}$	Stationary, i.e. non-rotating
$\square_{w}$	Wall

Abbreviations

CFD	Computational Fluid Dynamics
EXP	Experiment
GCI	Grid Convergence Index
LE	Leading Edge
PS	Pressure Side
RANS	Reynolds-averaged Navier-Stokes
SS	Suction Side
SST	Shear Stress Transport
TC	Thermocouple
TLC	Thermochromic Liquid Crystal

Acknowledgements

We are deeply grateful for the invaluable contributions of Prof. Dr.-Ing. Jens von Wolfersdorf, who was actively involved in this work until shortly before his passing. His expertise, mentorship, and passion for research will be greatly missed. We dedicate this paper to his memory. In addition to the authors listed for this paper, the following students of the University of Stuttgart have contributed to the experimental evaluation: Fabrizio Turco, Lisa Bogale and Bernabé Lorenzo Ávila; and to the numerical part of the work: Julian Reich.

Funding sources

The investigations were conducted as part of the joint research program RoboFlex-Turbo AP 3.1 in the frame of AG Turbo. The work was supported by the Bundesministerium fuer Wirtschaft und Energie as per resolution of the German Federal Parliament under grant number 03EE5013C. The authors gratefully acknowledge AG Turbo and MTU Aero Engines for their support and permission to publish this paper.

Competing interests

All authors declare that they have no conflict of interest.

References

ANSYS CFX Theory guide (2021). Release 2021 R2, ANSYS Inc.

ANSYS ICEM CFD User's manuals (2021). Release 2021 R2, ANSYS Inc.

Celik I., Ghia U., Roache P., Freitas C., Coloman H., and Raad P. (2008). Procedure for estimation and reporting of uncertainty due to discretization in CFD applications. *Journal of Fluids Engineering*. 130: 078001. https://doi.org/10.1115/1.2960953.

Ekkad S. V. and Singh P. (2021a). Detailed heat transfer measurements for rotating turbulent flows in gas turbine systems. *Energies*. 14 (1): 8. https://doi.org/10.3390/en14010039.

Ekkad S. V. and Singh P. (2021b). Liquid crystal thermography in gas turbine heat transfer: a review on measurement techniques and recent investigations. *Crystals*. 11 (11): 1332. https://doi.org/10.3390/cryst11111332.

Göhring M., Krille T., Feile J., and Wolfersdorf J. V. (2016). Heat transfer predictions in smooth and ribbed two-pass cooling channels under stationary and rotating conditions. In: 16th International Symposium on Transport Phenomena and Dynamics of Rotating Machinery, Honolulu, United States. https://hal.archives-ouvertes.fr/hal-01884254.

Göhring M., Hartmann C., and von Wolfersdorf J. (2018). Numerical investigation of transient heat transfer experiments under rotation, In: Vol. Volume 5A: Heat Transfer of Turbo Expo: Power for Land, Sea, and Air. https://doi.org/10.1115/GT2018-76497.

Gutiérrez de Arcos D., Waidmann C., Poser R., von Wolfersdorf J., and Jäppelt B. (2022). Comparison of experimental and numerical local rotational heat transfer effects in a two-pass cooling channel configuration. In: GT2022, Volume 6B: Heat Transfer — General Interest/Additive Manufacturing Impacts on Heat Transfer; Internal Air Systems; Internal Cooling. V06BT15A008. https://doi.org/10.1115/GT2022-79846.

Gutiérrez de Arcos D., Waidmann C., Poser R., von Wolfersdorf J., and Göhring M. (2024). Rotationally induced local heat transfer features in a two-pass cooling channel: experimental–numerical investigation. *International Journal of Turbomachinery, Propulsion and Power*. 9 (4): 17–21. https://doi.org/10.3390/ijtpp9040034.

Han J.-C. (2013). Fundamental gas turbine heat transfer. *Journal of Thermal Science and Engineering Applications*. 5 (2): 9. https://doi.org/10.1115/1.4023826.

Incropera F. P., DeWitt D. P., Bergman T. L., and Lavine A. S. (2017). Principles of heat and mass transfer, 8th edn, Global edition. New York: Wiley.

Ireland P. T. and Jones T. V. (2000). Liquid crystal measurements of heat transfer and surface shear stress. *Measurement Science and Technology*. 11 (7): 969–986. https://doi.org/10.1088/0957-0233/11/7/313.

Lorenzon A. and Casarsa L. (2020). Validation of the transient liquid crystal thermography technique for heat transfer measurements on a rotating cooling passage. *Energies*. 13 (18): 4759. https://doi.org/10.3390/en13184759.

Menter F. R. (1994). Two-equation eddy-viscosity turbulence models for engineering applications. *AIAA Journal*. 32 (8): 1598–1605. https://doi.org/10.2514/3.12149.

Poser R. and von Wolfersdorf J. (2010). Transient liquid crystal thermography in complex internal cooling systems, *VKI Lecture Series 2010-05, Internal Cooling in Turbomachinery, von Karman Institute for Fluid Dynamics*.

Poser R., von Wolfersdorf J., and Semmler K. (2005). Transient heat transfer experiments in complex passages. In: Heat Transfer Summer Conference, Vol. 47314, pp. 797–804.

Poser R., Von Wolfersdorf J., and Lutum E. (2007). Advanced evaluation of transient heat transfer experiments using thermochromic liquid crystals. *Proceedings of the Institution of Mechanical Engineers, Part A: Journal of Power and Energy*. 221 (6): 793–801. https://doi.org/10.1243/09576509JPE464.

Poser R., Ferguson J. R., and von Wolfersdorf J. (2009). Temporal signal preprocessing and evaluation of thermochromic liquid crystal indications in transient heat transfer experiments. In: 8th European Conference on Turbomachinery Fluid dynamics & Thermodynamics. European Turbomachinery Society, pp. 785–795.

Roache P. J. (1994). Perspective: a method for uniform reporting of grid refinement studies. *Journal of Fluids Engineering*. 116 (3): 405–413. https://doi.org/10.1115/1.2910291.

Shen Z., Xie Y., and Zhang D. (2015). Numerical predictions on fluid flow and heat transfer in U-shaped channel with the combination of ribs, dimples and protrusions under rotational effects. *International Journal of Heat and Mass Transfer*. 80: 494–512. https://doi.org/10.1016/j.ijheatmasstransfer.2014.09.057.

Wagner J. H., Johnson B. V., and Kopper F. C. (1991). Heat transfer in rotating serpentine passages with smooth walls. *Journal of Turbomachinery*. 113 (3): 321–330. https://doi.org/10.1115/1.2927879.

Waidmann C. (2020). Heat transfer measurements in rotating turbine blade cooling channel configurations using the transient thermochromic liquid crystal technique. PhD dissertation, University of Stuttgart.

Waidmann C., Poser R., and von Wolfersdorf J. (2013). Application of thermochromic liquid crystal mixtures for transient heat transfer measurements. In: 10th European Conference on Turbomachinery Fluid dynamics & Thermodynamics. European Turbomachinery Society.

Waidmann C., Poser R., Nieland S., and von Wolfersdorf J. (2016). Design of a rotating test rig for transient thermochromic liquid crystal heat transfer experiments. In: 16th International sSymposium on Transport Phenomena and Dynamics of Rotating Machinery, Honolulu, United States. https://hal.archives-ouvertes.fr/hal-01884257.

Waidmann C., Poser R., Göhring M., and Wolfersdorf J. V. (2018). First operation of a rotating test rig for transient thermochromic liquid crystal heat transfer experiments. In: XXIV Biannual Symposium on Measuring Techniques in Turbomachinery Transonic and Supersonic Flow in Cascades and Turbomachines.

Waidmann C., Poser R., Gutiérrez de Arcos D., Göhring M., von Wolfersdorf J., et al. (2022). Experimental investigation of local heat transfer in a rotating two-pass cooling channel using the transient thermochromic liquid crystal (TLC) technique. In: GT2022, Volume 6B: Heat Transfer — General Interest/Additive Manufacturing Impacts on Heat Transfer; Internal Air Systems; Internal Cooling. V06BT15A009. https://doi.org/10.1115/GT2022-81291.

White F. M. and Majdalani J. (2006). Viscous fluid flow, Vol. 3. New York: McGraw-Hill. Section: 1.

Williams W. C. (2011). If the Dittus and Boelter equation is really the McAdams equation, then should not the McAdams equation really be the Koo equation? *International Journal of Heat and Mass Transfer*. 54 (7): 1682–1683. https://doi.org/10.1016/j.ijheatmasstransfer.2010.11.047.